Multiscale modeling of lymphatic vasculature growth and adaptation

Rudolph L. Gleason Jr. Ph.D. [1,2,3], Alex Alexeev[2], and J. Brandon Dixon Ph.D.[1,2,3]

[1] Parker H. Petit Institute for Bioengineering and Bioscience, Georgia Institute of Technology 315 Ferst Dr. Atlanta, GA 30332
[2] George W. Woodruff School of Mechanical Engineering, Georgia Institute of Technology, 801 Ferst Dr. Atlanta, GA 30313
[3] Wallace H. Coulter Department of Biomedical Engineering, Georgia Institute of Technology, 313 Ferst Dr. NW, Atlanta, GA 30332

ABSTRACT

The lymphatic vasculature provides crucial functions for the maintenance of homeostasis in a variety of tissues and organs by providing the primary route through which immune cells, large proteins, lipids, and interstitial fluid are returned to the blood circulation. This requires the movement of fluid against an adverse pressure gradients, a process that is achieved primarily through the intrinsic contractility of individual contractile units known as lymphangions. Lymphatic pump failure has been implicated in a variety of disease processes including lymphedema, congestive heart failure, transplant rejection, and neurological disorders. All of these processes involve the growth and remodeling (G&R) of lymphatics as they adapt to changes directly from injury or to changes in the fluid demand placed upon them. These processes are quite complex, involving molecular mechanisms that adapt lymphatic function and structure across very short (seconds) and long (weeks) time scales. These changes that occur at the cellular level alter pump function of individual vessels at the tissue level, and ultimately could affect pump performance of the entire lymphatic network. Thus *a multiscale model that recapitulates these changes at the cellular level, integrating both the biological and mechanical variables important to the cell response, and then predicts their impact on the entire lymphatic network will be crucial to understanding disease progression and developing new therapies to restore lymphatic function.* Our work seeks to develop such a model, through a collaborative effort of three co-PIs with complementary expertise, utilizing both experimental and novel approaches in computational modeling. The first goal of this presentation is to describe a multiscale fluid-solid-growth model of individual lymphangions and chains of lymphangions in series. This model employs a 2D finite elastic model for the solid mechanics, a lumped parameter model of long lymphangion chains, and a volumetric growth model for the growth of the lymphangion. The second goal of this presentation is to describe a computational fluid-structure-interaction (FSI) model of a lymphatic valve. This model will develop an approach for capturing valve G&R processes through a coupled constrained mixture model of valve growth with a FSI model of complex fluid-valve interactions. Computational modeling results and experimental validation will be presented.

Constitutive Model

A. Constitutive Model for Passive Mechanical Response

$$T_{\theta\theta}^{pas} = 2C_{\theta\theta}^e \frac{\partial W}{\partial C_{\theta\theta}^e} - 2C_{rr}^e \frac{\partial W}{\partial C_{rr}^e} \qquad T_{zz}^{pas} = 2C_{zz}^e \frac{\partial W}{\partial C_{zz}^e} - 2C_{rr}^e \frac{\partial W}{\partial C_{rr}^e}$$

$$W = b(I_{C^e} - 3) + \sum_{k=1,2,3,4} \frac{b_1^k}{4b_2^k}\left\{ exp\left[b_2^k\left(\left(\lambda^k\right)^2 - 1\right)^2\right] - 1 \right\}$$
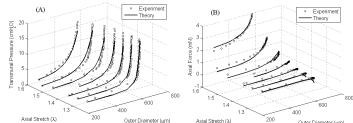
Figure 1: Left: Example passive biaxial mechanics showing model fit (lines) and experimental data (circles); Above: Fiber model is motivated from collagen microstructure of lymphatic vessel as visualized here using 2nd harmonic generation.

A. Constitutive Model for Active Contractile Response

$$T_{\theta\theta}^{act} = T_{act}\lambda_\theta^e\left[1 - \left(\frac{\lambda_M - \lambda_\theta^e}{\lambda_M - \lambda_0}\right)^2\right] \quad \text{and} \quad T_{zz}^{act} = 0 \quad T_{act} = \begin{cases} \frac{T_{phasic}}{2}\left[1 - cos\left(\frac{2\pi}{t_c}(t)\right)\right] + T_{tonic} \\ T_{tonic} \end{cases}$$
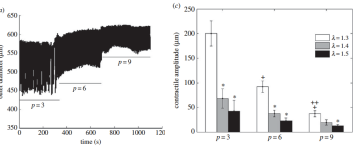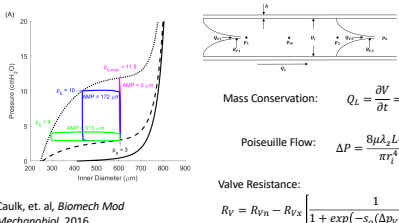
Figure 2: Left: Active contractile traces of lymphatic vessel under biaxial loading (λ=1.3). Right: Contractile data for collection of rat thoracic duct samples at 3 different pressures and 3 different axial loads. This data is fit with the active contractile equations in the model to determine T_{act}.

Integration into lumped parameter model

Adapted from Bertram, et. al, 2013

Mass Conservation: $Q_L = \frac{\partial V}{\partial t} = 2\pi r_i \frac{\partial r_i}{\partial t}\lambda_z L$

Poiseuille Flow: $\Delta P = \frac{8\mu\lambda_z LQ_L}{\pi r_i^4}$

Valve Resistance: $R_V = R_{Vn} - R_{Vx}\left[\frac{1}{1 + exp(-s_o(\Delta p_v - \Delta p_o))} - 1\right]$

Caulk, et. al, *Biomech Mod Mechanobiol*, 2016

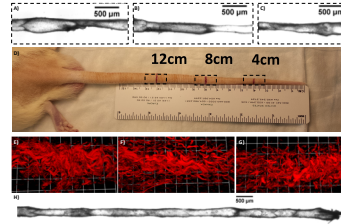## Lumped parameter model of lymphangion chains and validation in vivo

Figure 3: Geometric and microstructural properties of rat tail lymphatics along various regions of the tail. A–C: cannulated lymphatic vessels isolated from regions 12 cm (A), 8 cm (B), and 4 cm (C) from the tip of the tail, as shown in D. E–G: 2nd harmonic generation images of collagen microstructure of vessels isolated from regions 12 cm (E), 8 cm (F), and 4 cm (G) from the tip of the tail. H: chain of lymphangions showing typical valve spacing along the length of the chain.
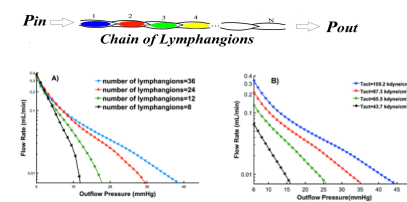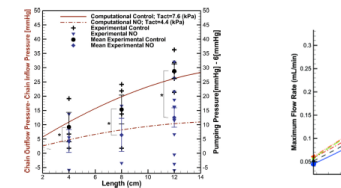
Figure 4: Flow rate as function of outflow pressure in the lymphangion chains. A: flow rates for different numbers of lymphangions in a chain with an activation parameter (Tact=10.9 kPa). B: flow rates for different values of Tact of smooth muscle cells in a chain with 36 lymphangions.

Figure 5: (Left): Effect of dermal nitric oxide (NO) delivery on the relationship between maximum outflow pressure and length from the tip of the tail using in vivo near-infrared imaging pumping pressure measurements and the computational model. The activation parameter associated with the degree of smooth muscle cell activation that best fits the in vivo NO experiments was found to be Tact 4.4 kPa. SEs along with the mean at 4 cm (n 4), 8 cm (n 3), and 12 cm (n 2) distance from the tip of the tail were plotted. Significant difference between the control and NO-treated data sets was determined using an extra sum of squares F-test on the quadratic best-fit regressions of the data (P 0.05). (Right): Maximum flow rate that can be achieved when there is no adverse pressure gradient present due to the intrinsic contraction of lymphangions with a different number of lymphangions in the chain as a function of lymphatic smooth muscle activation. Tact, activation parameter.

Figure 6: (A) Effect of refractory time on flow rate and maximum pressure in a chain of 8 lymphangions and (B) flow rate generated by intrinsic contraction of lymphangions for chains exposed to different opposing outflow pressures. (C): Effect of frequency on maximum pressure that can be overcome by a lymphangion chain to maintain flow rate determined by model for a chain of 8 lymphangions (Tact=10.9 kPa).

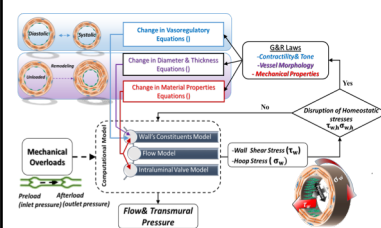## Computational Framework for Lymphatic Growth and Adaptation

Figure 7: Overview of G&R framework for lymphatics. When a mechanical load (inlet and outlet pressure) is placed on a lymphatic network, the immediate function of the vessel is determined by computational models describing systolic and tonic force generation of the contracting LMC (which are functions of both WSS and HS) and the passive mechanical properties of the vessel and valves. If the WSS and/or HS averaged over multiple contraction cycles differs from some target value, then G&R laws govern adjustment of both the passive and active properties of the vessel to restore homeostatic stress.
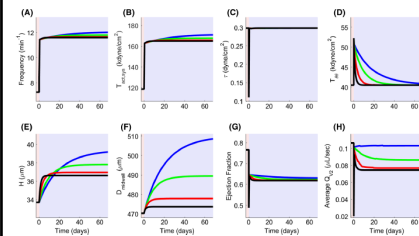
Figure 8: Change in contractile and mechanical parameters following acute contractile adaptation in response to a sustained increase in afterload. (A-B) Contractile frequency and systolic contractility increase following mechanical perturbation in order to restore shear stress. (C) Shear stress is restored to the homeostatic value following contractile adaptation. (D) Circumferential stress is reduced due but not restored by contractile adaptation. (E) ESD is decreased due to the increase in systolic contractility, which in turn increases the ejection fraction. (F) Average outflow is nearly restored to the pre-perturbation rate following contractile adaptation

Figure 9: Sensitivity analysis of the radial growth time constant in relation to volumetric growth and flow parameters. Radial growth time constants are 5 (black), 10 (red), 20 (green), and 30 (blue) days. (A-B) For a fixed value of circumferential growth rate, frequency and contractility increase as radial growth rate decreases. (C-D) Shear stress is continually maintained regardless of the radial growth rate, and circumferential stress is always restored but reaches homeostasis slower as radial growth rate decreases. (E-F) Unloaded thickness and midwall diameter experience progressively larger increases as radial growth rate decreases. The larger increase in diameter occurs to compensate for the slower radial growth rate in the process of restoring circumferential stress to homeostasis. (G-H) Ejection fraction and average outflow rate are decreased as the radial growth rate increases.
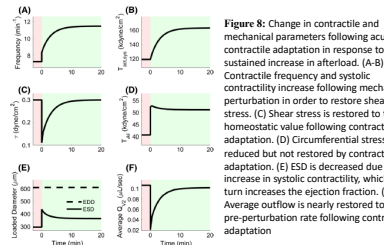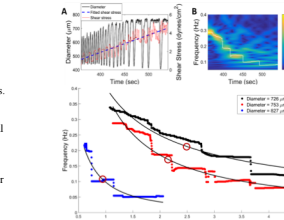
Figure 10: Experimental data of acute adaptations to WSS and their dependency on vessel diameter.
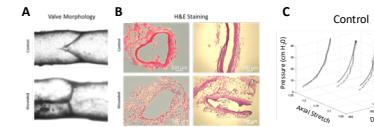
Large Animal Model of Lymphatic G&R

Figure 11: Remodeled vessels exhibit structural and mechanical alterations. A large animal model was developed where one of two vessels from a limb was excised and the compensatory vessel was allowed to undergo remodeling for 6 weeks. (A) The lymphatic valves of vessel segments from the wounded leg were prolapsed upon pressurization. (B) Vessel cross sections from the wounded leg (left column- transverse, right column- axial) have an increase in matrix surrounding the vessel. (C) Biaxial testing exhibited a decrease in vessel stiffness in remodeled vessels compared to control. The biaxial data (circles) was fit to a constitutive model (lines) to calculate material parameters that capture pressure-diameter behavior.

Figure 12: Computational simulation of lymphatic chain performance. Isolated vessel function and mechanical properties were utilized to inform a computational model, which was used to elucidate how the structural and functional changes caused by the surgery would affect intrinsically driven flow. A) Biaxial testing data was used to inform a computational model that predicts active and passive wall stress as a function of circumferential stretch. (B) (Left) Mechanical parameters coupled with ex-vivo isolated vessel flow rates as a function of the adverse pressure gradient. Pressure-volume curves for these simulations. (C) (Left) Mechanical parameters coupled with in-vivo contraction frequencies assessed via NIR imaging at day 42. (Right) Pressure-volume curves for these simulations.
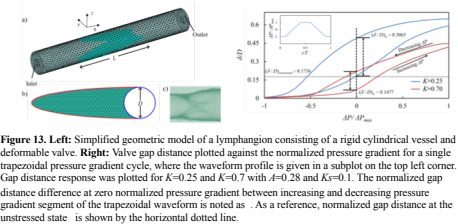
FSI Model of Lymphatic Valve

Figure 13: Left: Simplified geometric model of a lymphangion consisting of a rigid cylindrical vessel and deformable valve. **Right:** Valve gap distance plotted against the normalized pressure gradient for a single trapezoidal pressure gradient cycle, where the waveform profile is given in a subplot on the top left corner. Gap distance response was plotted for K=0.25 and K=0.7 with A=0.28 and Ks=0.1. The normalized gap distance difference at zero normalized pressure gradient between increasing and decreasing pressure gradient segment of the trapezoidal waveform is noted as . As a reference, normalized gap distance at the unstressed state is shown by the horizontal dotted line.
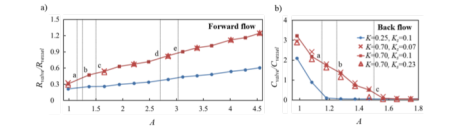
Figure 14: Plot of normalized valve resistance and conductance of lymphatic valves to forward and backward flow, respectively, for various aspect ratios A for a fixed vessel size and normalized stiffness values of K=0.25 and K=0.7. a) Normalized resistance to forward flow. Also note that Ks is varied between 0.07 and 0.23 selected values of A at K=0.7. b) Normalized conductance to back flow. Labels for d and e are not shown as the solution converges to zero for A>1.5.

ACKNOWLEDGEMENTS